



# The resolution dependence of optimal exposures in liquid nitrogen temperature electron cryomicroscopy of catalase crystals

Lindsay A. Baker<sup>a,b</sup>, Eric A. Smith<sup>a</sup>, Stephanie A. Bueler<sup>a</sup>, John L. Rubinstein<sup>a,b,\*</sup>

<sup>a</sup> Molecular Structure and Function Program, The Hospital for Sick Children Research Institute, Canada

<sup>b</sup> Department of Biochemistry, University of Toronto, Canada

## ARTICLE INFO

### Article history:

Received 17 September 2009

Received in revised form 20 November 2009

Accepted 25 November 2009

Available online 1 December 2009

### Keywords:

Electron cryomicroscopy

Radiation damage

Catalase

Optimal exposure

Critical exposure

## ABSTRACT

Electron beam damage is the fundamental limit to resolution in electron cryomicroscopy (cryo-EM) of frozen, hydrated specimens. Radiation damage increases with the number of electrons used to obtain an image and affects information at higher spatial frequencies before low-resolution information. For the experimentalist, a balance exists between electron exposures sufficient to obtain a useful signal-to-noise ratio (SNR) in images and exposures that limit the damage to structural features. In single particle cryo-EM this balance is particularly delicate: low-resolution features must be imaged with a sufficient SNR to allow image alignment so that high-resolution features recorded below the noise level can be recovered by averaging independent images. By measuring the fading of Fourier components from images obtained at 200 kV of thin crystals of catalase embedded in ice, we have determined the electron exposures that will maximize the SNR at resolutions between 86 and 2.9 Å. These data allow for a rational choice of exposure for single particle cryo-EM. For example, for 20 Å resolution, the SNR is maximized at  $\sim 20 \text{ e}^-/\text{Å}^2$ , whereas for 3 Å resolution, it is maximized at  $\sim 10 \text{ e}^-/\text{Å}^2$ . We illustrate the effects of exposure in single particle cryo-EM with data collected at  $\sim 12$ – $15$  and  $\sim 24$ – $30 \text{ e}^-/\text{Å}^2$ .

© 2009 Elsevier Inc. All rights reserved.

## 1. Introduction and rationale

Single particle electron cryomicroscopy (cryo-EM) of frozen, hydrated specimens is an increasingly important technique in the structural analysis of large protein complexes. In these experiments, macromolecular assemblies are embedded in a film of amorphous ice, preserving their structure even in the high vacuum of an electron microscope (Dubochet et al., 1988). The resolution limit of a modern electron microscope would allow for atomic resolution tomography of macromolecular assemblies were it not for the damage to biological specimens caused by the electron beam used to form the image. This damage occurs due to inelastic scattering of electrons from the specimen and is independent of the rate of irradiation, although reduced rates may decrease other undesirable phenomena, such as beam induced movement, sublimation, and specimen bubbling (Chen et al., 2008a,b). The loss of structural information is resolution-dependent: high-resolution details in a specimen are destroyed first while low-resolution features can tolerate significantly higher doses of absorbed energy (Glaeser, 1971; Conway et al., 1993). Cooling the specimen (Taylor and Glaeser, 1976) decreases beam-induced radiation damage and recent studies have sought to determine the optimal temperature

at which to conduct cryo-EM experiments (Comolli and Downing, 2005; Iancu et al., 2006; Wright et al., 2006; Bamme et al., 2010). In addition to cryoprotection, the total electron exposure used to obtain an image must be limited to avoid the destruction of the specimen. These low exposures result in images that have not built up the statistical significance necessary to observe high-resolution specimen features above image noise (Glaeser, 1971). For reasons that are not entirely clear, ice-embedded specimens have particularly poor contrast at high spatial frequencies (Henderson, 1992), further exacerbating the problem.

High-resolution structure determination for macromolecules attempts to restore this lost contrast by, where possible, averaging independent images of identical molecules to decrease the noise and reveal the signal. In cryo-EM of randomly oriented macromolecular assemblies, information at low spatial frequencies is used to determine the orientation of particle images relative to a reference volume. For these experiments, the microscopist must choose an exposure that balances the destruction of high-resolution features in the specimen with obtaining a SNR at low frequencies sufficient to determine orientation parameters. The use of too high an exposure or too low an exposure could prevent the construction of an accurate 3-D map or limit the resolution obtained in a map. The best strategy for choosing the total exposure of electrons to use in the experiment would be to select the highest possible exposure that still preserves with acceptable SNR the highest-resolution information that the experiment aims to extract from the images.

\* Corresponding author. Address: 555 University Avenue Toronto, Ontario, Canada M5G 1X8. Fax: +1 416 813 5022.

E-mail address: [john.rubinstein@utoronto.ca](mailto:john.rubinstein@utoronto.ca) (J.L. Rubinstein).

While it is difficult to use single particles to measure quantitatively the optimal exposure as a function of resolution, image series of thin crystals provide an efficient way to determine the best exposure. In electron tomography of frozen, hydrated specimens, an exposure must be chosen that balances information lost due to radiation damage and information lost due to poor imaging statistics. Analysis of radiation damage of thin crystals can also inform the choice of appropriate exposures in electron tomography.

Many studies have taken advantage of crystalline specimens to characterize electron beam damage (Chen et al., 2008a; Glaeser, 1971, 1979; Taylor and Glaeser, 1976; Bamme et al., 2010; Henderson, 1992; Hayward and Glaeser, 1979; Howitt et al., 1976; Unwin and Henderson, 1975; Stark et al., 1996). With a crystal specimen, direct recording of diffraction yields spots on a well-defined reciprocal space lattice. The position of a diffraction spot indicates the spatial frequency of the information that it conveys while the intensity of a spot is equal to the square of the amplitude of the Fourier component at that position. Similarly, Fourier transforms of images of crystals give the Fourier components directly, but the amplitudes of the Fourier components are scaled by the contrast transfer function (CTF) of the microscope.

During irradiation, the signal contributed to a Fourier component decreases steadily as the structural information is lost, leading to fading of the diffraction spot or calculated Fourier component. The fall-off of intensities can be modeled as an exponential function (Hayward and Glaeser, 1979; Unwin and Henderson, 1975) with

$$|f_{\vec{k}}(N)|^2 = |f_{\vec{k}}(0)|^2 e^{-N/N_e(\vec{k})}, \quad (1)$$

where  $N$  is the total accumulated electron exposure of the specimen,  $|f_{\vec{k}}(N)|^2$  is the instantaneous intensity at exposure  $N$  for a component with Fourier coordinates  $\vec{k}$ ,  $|f_{\vec{k}}(0)|^2$  is the initial instantaneous intensity of the component, and the total accumulated electron exposure at which the intensity of the component decreases to  $e^{-1}$  times its initial value (approximately 0.368) is defined as the critical exposure,  $N_e(\vec{k})$  (Unwin and Henderson, 1975). Even after fading to  $e^{-1}$  times its initial intensity, some continued addition to the signal occurs until the component has faded entirely. Furthermore, once recorded, information about high-resolution features remains in an image even if the features themselves are destroyed in the specimen. The optimal exposure to maximize the SNR in an image for a spatial frequency,  $N_{opt}(\vec{k})$ , was determined to be  $\sim 2.5 N_e(\vec{k})$  in the absence of strong object and detector noise (Hayward and Glaeser, 1979). For direct recording of electron diffraction, the optimal exposure to use is usually only slightly higher than  $N_e(\vec{k})$  (Downing and Li, 2001).

Early experiments determined  $N_e(\vec{k})$  and  $N_{opt}(\vec{k})$  for unstained specimens by following diffraction spots with resolutions between 11.7 and 4.0 Å (Hayward and Glaeser, 1979). For many single particle EM studies, particularly for asymmetric particles, these resolutions are still considered ambitious, and for electron cryotomography, these resolutions are almost certainly beyond what can be achieved from a single tomogram (Rosenthal and Henderson, 2003). Therefore, we have followed the radiation damage in cryo-EM images of catalase crystals preserved at liquid nitrogen temperature for resolutions between 86 and 2.9 Å. We have performed these experiments using a 200 kV electron microscope equipped with a field emission gun, one of the most common instruments used for single particle cryo-EM. For 521 different Fourier components, we determined  $N_e(\vec{k})$  and  $N_{opt}(\vec{k})$  and combined this information to determine the optimal exposure as a function of spatial frequency. These data will allow anyone working with similar imaging conditions to quickly determine the highest possible exposure that will still preserve the information they strive to obtain in their final 3-D map. The results suggest that

many earlier studies have not used optimal electron exposures for image acquisition.

## 2. Materials and methods

### 2.1. Specimen preparation

Thin crystals of catalase were grown as described previously (Dorset and Parsons, 1975). Briefly, dehydrated bovine liver catalase (Sigma–Aldrich Canada Ltd., Oakville, ON) at 60–100 mg/ml was resuspended in buffer containing 28 mM  $\text{Na}_2\text{HPO}_4$  and 5 mM  $\text{KH}_2\text{PO}_4$  (pH 7.4). The pH of the suspension was adjusted to 5.3 with saturated  $\text{KH}_2\text{PO}_4$  and the sample was incubated at 4 °C for several weeks to allow crystal growth. Immediately prior to grid preparation for cryomicroscopy, the catalase suspension was mixed and a sample was withdrawn from the slurry. The sample was washed twice with water before resuspending in one volume of cold water.

### 2.2. Electron microscopy

Cryo-EM specimens were prepared with a Vitrobot grid preparation robot (FEI Company, Eindhoven, Netherlands) on freshly glow discharged EM grids covered with a continuous carbon film for crystals and freshly washed and glow discharged Quantifoil R2/2 grids (Quantifoil MicroTools GmbH, Germany) for single particles. Specimens were imaged with a Tecnai F20 microscope (FEI Company) equipped with a field emission gun and operating at 200 kV, 50000 × magnification, and with nominal defoci between 200 and 400 nm for crystals and 3 and 6 μm for single particles. The temperature of the specimen was measured using the Smart Set Cold Stage Controller (Gatan Inc., Warrendale, PA, USA) as −169 °C. Imaging was performed in low dose mode and electron exposures were measured with the exposure calibration function of the microscope. This function calculates the electron exposure from the magnification of the microscope, the electrical current through the viewing screen, and the efficiency of the screen at capturing electrons. The electron capture efficiency of the screen at 200 kV was determined when the microscope was manufactured. Electron exposures were measured using regions of the specimen grid where there was no carbon film so that the scattering of electrons from the sample would not complicate the calculation. For crystals, image series were recorded at constant defocus with 5–15  $\text{e}^-/\text{Å}^2$  on the specimen per image and with a beam blank of  $\sim 20$  s between exposures. Single particle data was collected with exposures of 12–15  $\text{e}^-/\text{Å}^2$  or 24–30  $\text{e}^-/\text{Å}^2$ . Images were recorded on SO-163 electron film (Kodak Canada, Toronto, ON) and developed for 4–30 min in full strength Kodak D19.

### 2.3. Image processing

Micrographs were digitized with an Intergraph Photoscan densitometer (Intergraph, Huntsville, Alabama, USA) using a 7 μm step size, giving an effective pixel size of 1.4 Å. Images of crystals were selected and windowed to 3000 × 3000 pixels with the MRC image analysis software (Crowther et al., 1996). Subsequent analysis and lattice refinement were performed with the 2dx software package (Gipson et al., 2007), making use of now standard 2-D crystal processing techniques (Henderson et al., 1990). The uncertainty in intensity measurements was taken as the variance of the background intensities surrounding the Fourier components. The uncertainties in the critical exposures were calculated using standard error propagation methods (Taylor, 1999). Images of single particles were compressed fourfold, giving an effective pixel size of 5.6 Å on the specimen, and CTF parameter determination was

performed with CTFFIND3 (Mindell and Grigorieff, 2003). Individual particles were selected and windowed to  $64 \times 64$  pixels with the MRC image analysis software. The different sets of particle images were used to refine a previously published map of ATP synthase (Rubinstein et al., 2003) (EMDB # 1357) with FREALIGN version 5 (Grigorieff, 2007) using random starts (mode 4, DANG = 210, ITMAX = 200) for three iterations of alignment and model construction. Single particles were masked (RI) with a radius of 120.0 Å and resolutions between 240.0 and 42.0 Å were used for alignment. No model mask (XSTD = 0.0) or B factor (RBFAC = 0.0) was used during alignment.

### 3. Results and discussion

Catalase crystals were imaged in series at constant defocus. Five series were chosen where the crystal in the first image showed a

well-ordered lattice. The same area was selected from each micrograph in each series and processed with the MRC image analysis programs (Crowther et al., 1996; Henderson et al., 1990) through the 2dx software package (Gipson et al., 2007). A sample of the computed diffraction patterns is shown in Fig. 1a–d. The Nyquist–Shannon information limit for this combination of magnification and densitometer step size is 2.8 Å. To assess the reliability of the Fourier components, the *IQ* parameter was used (Henderson et al., 1986). The value of the parameter is given by  $IQ = 7(B/A)$ , where *A* is the background corrected amplitude of the component and *B* is the background near the component (Henderson et al., 1990). Fourier components with *IQ* values of 4 or less, which represent highly reliable data (Glaeser et al., 2007), were present past 2.9 Å resolution in some images.

From Eq. (1), it can be seen that a plot of  $\ln(|f_{\vec{k}}|^2)$  versus  $N$  should have a slope of  $-1/N_e(\vec{k})$  and y-intercept of  $\ln |f_{\vec{k}}(0)|^2$ , allowing for straightforward determination of the critical exposure for a

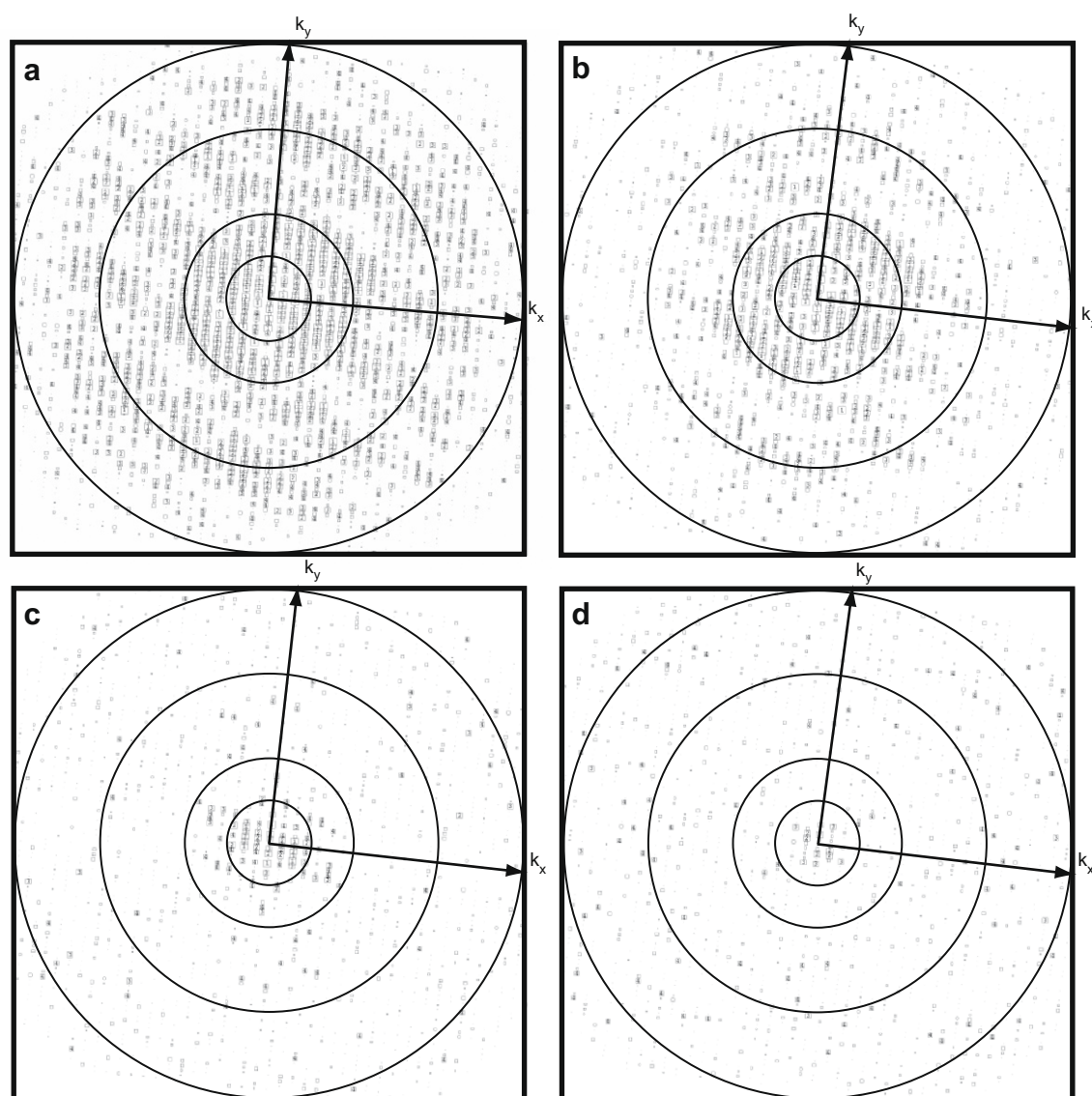


**Fig. 1.** Fourier component *IQ* values as a function of exposure for an example image series. The sizes of the boxes are proportional to the quality of the Fourier components, as measured by *IQ* values, with larger boxes corresponding to lower *IQ* values. In order of increasing radius, the circles in each panel represent 20, 10, 5, and 3.3 Å resolution, respectively. In this series, an exposure of  $8 \text{ e}^-/\text{Å}^2$  was used to acquire the images from which the patterns were calculated. The lunes observed in the diffraction pattern arise from a slight tilt in the crystal ( $<3^\circ$ ), which contains more than one monolayer of protein (Jesior, 1982). (a) The Fourier transform from the first image in the series, acquired with a total exposure of  $8 \text{ e}^-/\text{Å}^2$  on the specimen. (b) The Fourier transform from an image of the same area of crystal, acquired with an additional  $8 \text{ e}^-/\text{Å}^2$  for a total exposure of  $16 \text{ e}^-/\text{Å}^2$ . (c) The same area, previously irradiated with  $46 \text{ e}^-/\text{Å}^2$ , imaged with an accumulated exposure of  $54 \text{ e}^-/\text{Å}^2$ . (d) The same area from an image acquired with  $8 \text{ e}^-/\text{Å}^2$  after  $78 \text{ e}^-/\text{Å}^2$  of pre-exposure for a total accumulated exposure of  $96 \text{ e}^-/\text{Å}^2$ .



Fourier component. However, direct measurements of the instantaneous intensity cannot be made because any real detector, including film, must be given a finite exposure of electrons in order to record an image. Therefore, from a real detector, the intensity measured is  $|F_{\vec{k}}(N, \Delta N)|^2$ , where  $N - \Delta N$  is the total accumulated exposure that the specimen has been subjected to before beginning imaging and  $N$  is the total accumulated exposure of the specimen by the end of the image. As shown below, these data can still be used to determine values for  $N_e(\vec{k})$ . If imaging is assumed to be linear with exposure, then

$$P_{\vec{x}}(N, \Delta N) = C \int_{N-\Delta N}^N \rho_{\vec{x}}(n) dn, \quad (2)$$

where  $P_{\vec{x}}(N, \Delta N)$  is the image recorded as a function of spatial coordinates  $\vec{x}$ , with an exposure acquired between  $N - \Delta N$  and  $N$  electrons,  $\rho_{\vec{x}}(n)$  is the instantaneous image at exposure  $n$ , and  $C$  is a scaling factor that depends on the response of the detector. A linear imaging process implies that the Fourier transform is also linear, such that

$$F_{\vec{k}}(N, \Delta N) = C \int_{N-\Delta N}^N f_{\vec{k}}(n) dn. \quad (3)$$

Here,  $F_{\vec{k}}(N, \Delta N)$  is a Fourier component with spatial frequency coordinates  $\vec{k}$  from an image recorded with exposure  $\Delta N$ , up to a total exposure of  $N$  on the specimen, and  $f_{\vec{k}}(n)$  is an instantaneous measurement of the component of the Fourier transform produced at exposure  $n$ . From Eq. (1) it can be seen that the fading of amplitudes of Fourier components is also exponential with exposure, such that

$$|F_{\vec{k}}(N, \Delta N)| = C \int_{N-\Delta N}^N |f_{\vec{k}}(0)| e^{-\frac{n}{2N_e(\vec{k})}} dn, \quad (4)$$

where  $|f_{\vec{k}}(0)|$  is the instantaneous amplitude of the Fourier component prior to any radiation damage. The factor of two in the denominator of the exponential arises from consideration of amplitudes instead of intensities. The expression can be evaluated and squared, and written in terms of natural logarithms to make it linear with total accumulated exposure,  $N$ :

$$\ln(|F_{\vec{k}}(N, \Delta N)|^2) = \frac{-1}{N_e(\vec{k})} \cdot N + 2 \ln \left[ 2N_e(\vec{k})C|f_{\vec{k}}(0)| \cdot \left( e^{\frac{\Delta N}{2N_e(\vec{k})}} - 1 \right) \right] \quad (5)$$

Therefore, for images obtained with an exposure between  $N - \Delta N$  and  $N$  electrons per unit area, a plot of the natural logarithm of intensity values for a Fourier component versus  $N$  yields a straight line with slope  $-1/N_e(\vec{k})$ , although the  $y$ -intercept is no longer  $|f_{\vec{k}}(0)|^2$ .

To calculate critical exposures, weighted linear regressions were performed on logarithmic plots of integrated intensity values as a function of accumulated exposure for 1051 Fourier components with initial  $IQ \leq 4$  (Fig. 2). Of these, critical exposures from the 521 Fourier components that gave the most reliable regressions were used in subsequent analysis.

The Fourier components from each image series were sorted into 64 bins according to the reciprocal space sampling of a discrete Fourier transform of 128 samples of the same size as the pixels in the images. The fastest fading Fourier component from each bin in each series was selected and data were combined from the five different exposure series, each of 6–12 micrographs, by averaging the critical exposures in corresponding bins to produce a plot of critical exposure and optimal exposure as a function of resolution (Fig. 3). The plot in Fig. 3 allows for selection of an exposure to maximize the SNR at any resolution. Although the amount of radiation damage per useful elastic interaction is not expected to change between 200 and 300 kV (Henderson, 1995), at 300 kV an exposure that is  $\sim 25\%$  higher would be required for the same num-

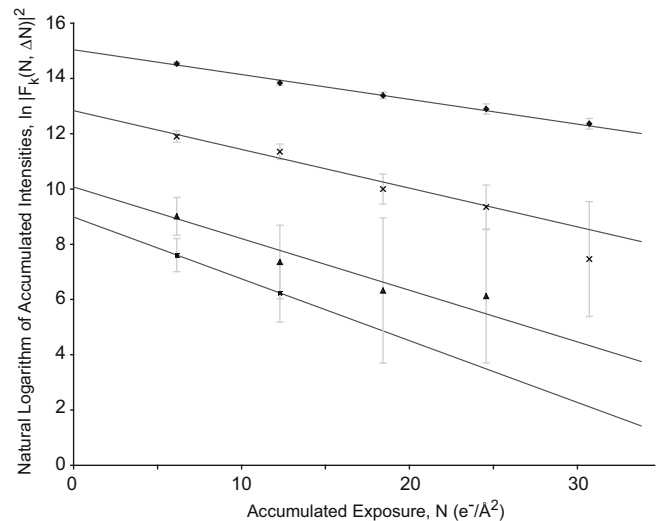


**Fig. 2.** Determination of critical exposure,  $N_e(\vec{k})$ , for individual Fourier components. Weighted linear regressions (solid lines) of the natural logarithms of intensities as a function of accumulated exposure were calculated for Fourier components at different resolutions. Examples are shown for components at 2.9 Å (■), 6.1 Å (▲), 15.5 Å (×), and 37 Å (◆). The slope of each line is equal to  $-1/N_e(\vec{k})$ , as shown in Eq. (5).

ber of elastic interactions to occur (Yalcin et al., 2006), resulting in higher critical and optimal exposures at that voltage.

For our experiments, the catalase crystals were supported by a thin film of continuous carbon. It is thought that carbon films may reduce specimen charging when compared to protein in unsupported vitreous ice (Brink et al., 1998). However, analysis of radiation damage in catalase crystals prepared over holes in a perforated carbon film coated EM grid (Bammes et al., 2010) resulted in slightly higher critical exposures than our study. These higher exposures, even when one accounts for the 300 kV electron beam used in that experiment, suggest that specimen charging is not a significant factor in the measurement of critical and optimal exposures. Charging of the specimen may also be decreased by obtaining an image of equal exposure but produced with lower electron flux over a longer time. However, no significant difference in critical exposure was calculated from images obtained with  $5 \text{ e}^-/\text{Å}^2$  and  $10 \text{ e}^-/\text{Å}^2$  exposure of the specimen, suggesting that fractionating the exposure differently does not affect the rate of information loss observed.

The optimal exposures determined here are somewhat higher than would be suggested from experiments with models built from pre-irradiated specimens, where the highest-resolution information is completely lost by the time the image is recorded (Conway et al., 1993). Earlier studies that determined critical exposures did so only for high-resolution Fourier components ( $\leq 12 \text{ Å}$ ) (Taylor and Glaeser, 1976; Hayward and Glaeser, 1979; Unwin and Henderson, 1975; Knapek and Dubochet, 1980) and used electron accelerating voltages (e.g. 100 kV) and temperatures (room temperature or  $-120^\circ\text{C}$ ) no longer common for studying unstained specimens. The difference in accelerating voltage can be accounted for by considering the scattering cross-sections at different energies, which should allow for a  $\sim 40\%$  lower exposure at 100 kV. For the study most similar to the one presented here (Hayward and Glaeser, 1979), the adjusted critical exposures agree well with our measurements between 2.9 and 5 Å, although at lower resolutions, the critical exposures we report in Fig. 3 are smaller.

There are three important considerations for the interpretation of the curves in Fig. 3. The first caveat is that specimen bubbling, probably due to the production of hydrogen gas following radiolysis of water, may interfere with image acquisition at extremely

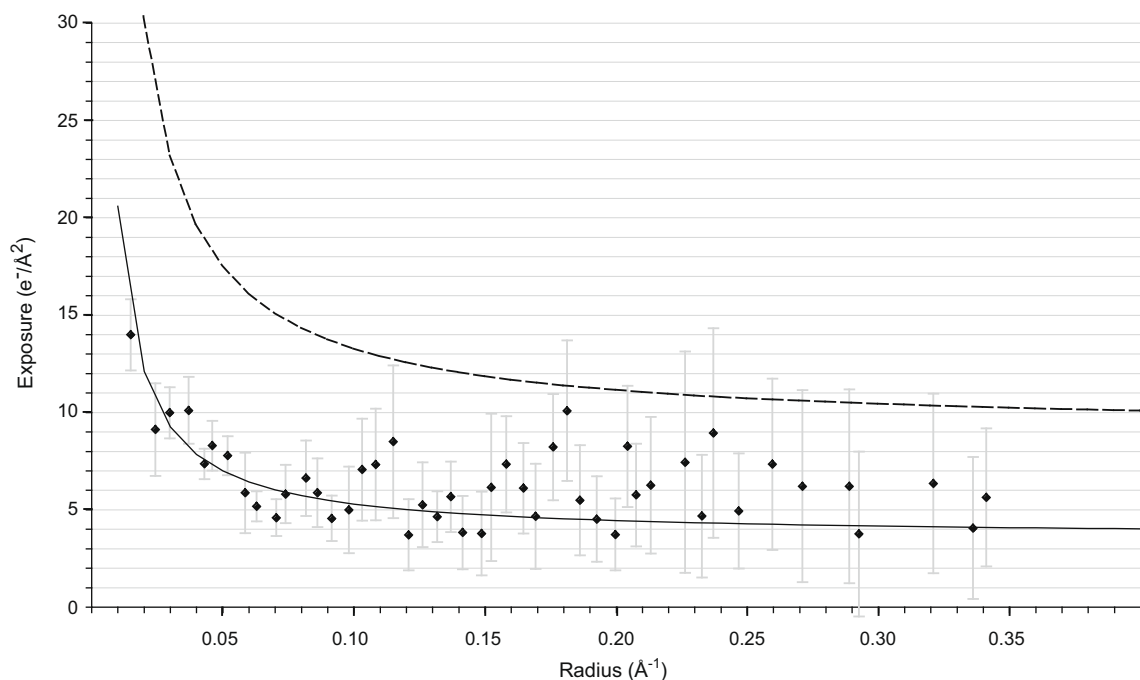


**Fig. 3.** Critical and optimal exposures at 200 kV as a function of radius in Fourier space. In five different image series, the fastest fading Fourier component in each of 64 resolution bins was identified and its critical exposure determined. The average critical exposure for each resolution bin was calculated from all image series. The larger uncertainties at higher resolutions are a result of the difficulties inherent in the measurement of low intensity Fourier components, compounded by the nature of the logarithmic transformation. The experimental critical exposures (points) were fit as a function of resolution (i.e. the inverse of the distance of the resolution bin from the centre of the Fourier transform) with a weighted linear regression for bins between 80 and 5 Å (solid line). The data had a Pearson's coefficient of 0.75, which, for the size of the data set, indicates less than a 0.05% probability that the data is uncorrelated (Taylor, 1999). The fit of the critical exposure with Fourier radius was used to plot an expected optimal exposure curve (dashed line) at 2.5 times the critical exposure, based on the relationship derived by Hayward and Glaeser (1979). This optimal exposure estimate assumes minimal detector and structural noise; for real samples and detectors, the optimal exposure is probably slightly lower. At 300 kV, 120 kV, and 100 kV, critical and optimal exposures would be ~25% higher, ~30% lower, and ~40% lower, respectively (Henderson, 1995; Yalcin et al., 2006).

high exposures, making these exposures undesirable. We tested for the point of bubble formation in cryo-specimens under the standard conditions that we described. We found that bubbling occurred in ice over carbon between 30 and 45  $\text{e}^-/\text{\AA}^2$ , but we could not see bubbling in ice over holes in a grid before 150  $\text{e}^-/\text{\AA}^2$ . It is commonly observed that the inclusion of organic additives with a specimen can reduce the exposure at which bubbling occurs, and these additives should be avoided when preparing cryo-EM grids. If organic additives are used for preparing EM grids, they could reduce the electron exposures that are optimal for an experiment. The second consideration has already been pointed out by Hayward and Glaeser (1979). From Hayward and Glaeser, the expression for SNR at a given resolution in the absence of strong detector and structure noise is

$$\text{SNR}_k(N) \propto \frac{(1 - e^{-N/2N_e(k)})^2}{N} \quad (6)$$

This curve shows a rapid increase in SNR with increasing exposures up to  $N_{\text{opt}}(k)$ , followed by a gradual decrease in SNR beyond  $N_{\text{opt}}(k)$ . Therefore, to maximize SNR at a specific spatial frequency, it is usually preferable to slightly over-irradiate the specimen rather than under-irradiate it. Fig. 4 shows the SNR for several resolutions as a function of total accumulated exposure. Finally, when atomic resolution structures are desired, it should be recognized that high electron exposures can change the chemical structure of the specimen, initially affecting cysteine, aspartate, and glutamate residues (Ravelli and McSweeney, 2000). Chemical changes to macromolecular structure can occur as early as 0.1  $\text{e}^-/\text{\AA}^2$  (Henderson, 2004; Matsui et al., 2002), and would need to be accounted for in high-resolution models.

Taking the above issues into account, one can use the data in Fig. 3 and curves like those in Fig. 4 to select an exposure for use in an imaging experiment. For single particle experiments, for high-resolution studies (e.g. 3–5 Å resolution) of symmetric particles, such as viruses, where determination of orientation parameters for particle images is quite robust, one could use an exposure of approximately 10  $\text{e}^-/\text{\AA}^2$  to maximize the SNR for high-spatial frequencies. For high-resolution studies of smaller particles, where good SNRs for frequencies between 100 and 20 Å are necessary for alignment, a somewhat higher exposure of 15–25  $\text{e}^-/\text{\AA}^2$  could be used. This exposure will improve the SNR of the low spatial frequencies, but at the expense of a ~10% decrease in the SNR for the high-resolution information. For studies where the goal is to build a 3-D model at modest resolution, a significantly higher exposure of electrons, such as 30  $\text{e}^-/\text{\AA}^2$ , could be used to maximize the chances of success, as long as this exposure does not lead to bubbling in the specimen. The critical exposures that we measured for low-resolution Fourier components can also be used to inform the choice of exposure in electron tomography. However, it is not clear what the relationship is between critical exposure and the optimal cumulative exposure in a tilt series. Finally, the curve in Fig. 3 suggests that at 200 kV and liquid nitrogen temperature, exposures lower than ~10  $\text{e}^-/\text{\AA}^2$  are unnecessarily conservative for almost any imaging experiment. The shape of the curve in Fig. 3 at high resolution is consistent with other recent studies of radiation damage (Bammes et al., 2010). The critical exposures that we have determined suggest that many moderate resolution single particle studies, including our own (Rubinstein et al., 2003; Lau et al., 2008), have been performed with unnecessarily conservative electron exposures that may have reduced the accuracy of image to model alignment.

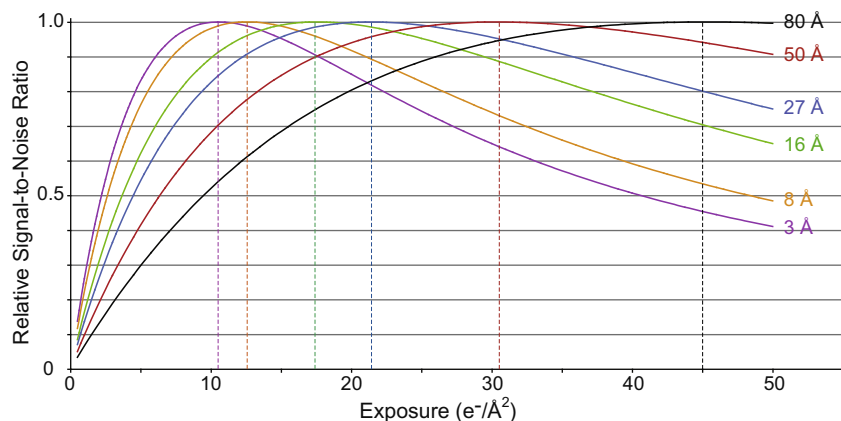


**Fig. 4.** Relative signal-to-noise ratio as a function of exposure at 200 kV. Signal-to-noise ratios (SNRs), scaled between 0 and 1, are plotted for different resolutions as a function of exposure, as described in Eq. (6). Determination of the best exposure for an imaging experiment will involve a compromise between maximizing the SNR at lower resolutions while maintaining sufficient SNR at the highest resolution of interest to the experiment. An exposure of  $N_e(\bar{k})$  will result in a relative signal-to-noise ratio of 0.4 at any given spatial frequency. The dotted vertical lines indicate the maximum,  $N_{opt}(\bar{k})$ , for each curve.

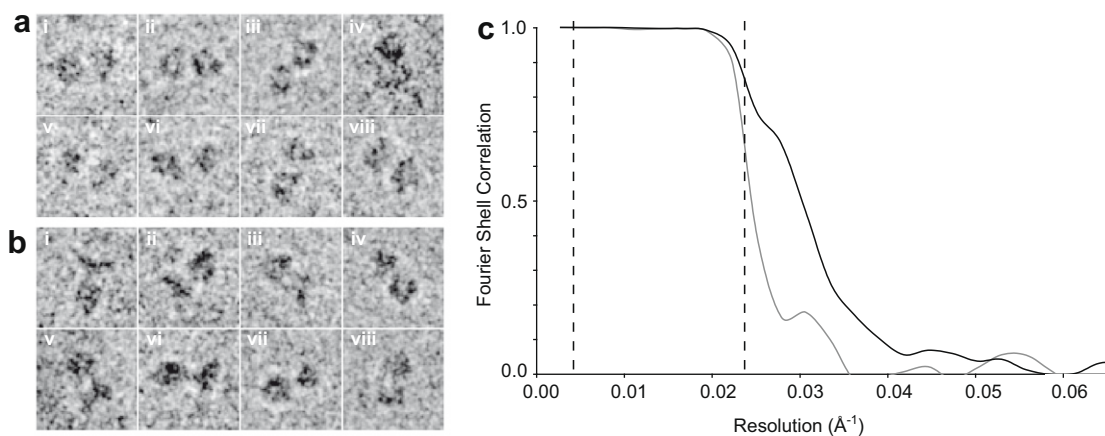


**Fig. 5.** Single particle map refinement with cryo-EM images acquired with different exposures. Test data sets of 5000 images each of ATP synthase particles were collected with exposures of either  $\sim 12\text{--}15\text{ e}^-/\text{\AA}^2$  or  $\sim 24\text{--}30\text{ e}^-/\text{\AA}^2$ . Subtle differences between the data sets can be seen in examples of single particle images, as shown in part **a** (i–viii) for the  $\sim 12\text{--}15\text{ e}^-/\text{\AA}^2$  data and in part **b** (i–viii) for  $\sim 24\text{--}30\text{ e}^-/\text{\AA}^2$  data. A previously published map of ATP synthase (Rubinstein et al., 2003) was refined with these data sets using FREALIGN (Grigorieff, 2007). Fourier shell correlation functions are shown in part **c** for the map refined with  $\sim 12\text{--}15\text{ e}^-/\text{\AA}^2$  data (grey line) and the map refined with  $\sim 24\text{--}30\text{ e}^-/\text{\AA}^2$  (black line). The dotted lines indicate the resolution range used in refinement.

To illustrate the effect of imaging exposure on 3-D map quality in single particle EM, we collected two datasets from bovine ATP synthase, each consisting of 5000 single particle images. One dataset was collected with exposures of  $\sim 12\text{--}15\text{ e}^-/\text{\AA}^2$  on the specimen and the other exposures of  $\sim 24\text{--}30\text{ e}^-/\text{\AA}^2$  (Fig. 5a and b). A previously published 3-D map of ATP synthase (Rubinstein et al., 2003) was refined with these datasets. The Fourier shell correlation curves (Fig. 5c) after refinement clearly show that the higher exposure dataset performs better than the lower exposure images. The improvement observed with the higher exposure dataset probably arises from two sources: first, the improved SNR at lower spatial frequency allows for more accurate alignment of images; and second, at the moderate resolutions obtained for these maps of ATP synthase, increasing the exposure of electrons improves the SNR of particle images at the resolution limit of the map.

These results also have an additional application. New image detectors offer the possibility of capturing many frames during the imaging process (Faruqi and Henderson, 2007), making each image an exposure series. With these detectors, the first few frames would record high spatial frequencies from the specimen with maximal SNRs. In comparison, an average of many frames would have low SNRs for the high-resolution information but would record low spatial frequencies with high SNRs. This average of many

frames would allow for accurate alignment of particle images while the first few frames could be used to build high-resolution models. An even more sophisticated approach would be to use the optimal exposures measured here to calculate weighted averages of frames in order to maximize the SNR at each spatial frequency.

#### 4. Statement of contributions

JLR conceived the study and JLR and LAB designed the experiments; SAB established the catalase crystal growth conditions; LAB and EAS prepared the cryo-EM specimens, collected the cryo-EM data, and analyzed the images; LAB performed the single particle EM experiments and data analysis; JLR advised on all aspects of the project; and JLR and LAB wrote the manuscript. JLR and LAB are guarantors for this work.

#### Acknowledgments

We thank Richard Henderson and Peter Rosenthal for valuable discussions and a critical reading of this manuscript. LAB was supported by a Vanier Canada Graduate Scholarship from the NSERC, EAS was supported by a SSuRe studentship from SickKids, and

JLR was supported by a New Investigator Award from the CIHR and an Early Researcher Award from the Ontario Ministry of Research and Innovation. This research was funded by operating grant MOP 81294 to JLR from the CIHR.

## References

- Bammes, B.E., Jakana, J., Schmid, M.F., Chiu, W., 2010. Radiation damage effects at four specimen temperatures from 4 K to 100 K. *J. Struct. Biol.* 169, 331–341.
- Brink, J., Sherman, M.B., Berriman, J., Chiu, W., 1998. Evaluation of charging on macromolecules in electron cryomicroscopy. *Ultramicroscopy* 72, 41–52.
- Chen, J.Z., Sachse, C., Xu, C., Mielke, T., Spahn, C.M., Grigorieff, N., 2008a. A dose-rate effect in single-particle electron microscopy. *J. Struct. Biol.* 161, 92–100.
- Chen, J.Z., Sachse, C., Xu, C., Mielke, T., Spahn, C.M., Grigorieff, N., 2008b. Corrigendum to: a dose-rate effect in single-particle electron microscopy. *J. Struct. Biol.* 164, 240.
- Comolli, L.R., Downing, K.H., 2005. Dose tolerance at helium and nitrogen temperatures for whole cell electron tomography. *J. Struct. Biol.* 152, 149–156.
- Conway, J.F., Trus, B.L., Booy, F.P., Newcomb, W.W., Brown, J.C., Steven, A.C., 1993. The effects of radiation damage on the structure of frozen hydrated HSV-1 capsids. *J. Struct. Biol.* 111, 222–233.
- Crowther, R.A., Henderson, R., Smith, J.M., 1996. MRC image processing programs. *J. Struct. Biol.* 116, 9–16.
- Dorset, D.L., Parsons, D.F., 1975. Electron diffraction from single, fully-hydrated. Ox-Liver Catalase Microcrystals *Acta Cryst.* A31, 210–215.
- Downing, K.H., Li, H., 2001. Accurate recording and measurement of electron diffraction data in structural and difference fourier studies of proteins. *Microsc. Microanal.* 7, 407–417.
- Dubochet, J., Adrian, M., Chang, J.J., Homo, J.C., Lepault, J., McDowell, A.W., Schultz, P., 1988. Cryo-electron microscopy of vitrified specimens. *Q. Rev. Biophys.* 21, 129–228.
- Faruqi, A.R., Henderson, R., 2007. Electronic detectors for electron microscopy. *Curr. Opin. Struct. Biol.* 17, 549–555.
- Gipson, B., Zeng, X., Zhang, Z.Y., Stahlberg, H., 2007. 2dx – user-friendly image processing for 2D crystals. *J. Struct. Biol.* 157, 64–72.
- Glaeser, R.M., 1971. Limitations to significant information in biological electron microscopy as a result of radiation damage. *J. Ultrastruct. Res.* 36, 466–482.
- Glaeser, R.M., 1979. Prospects for extending the resolution limit of the electron microscope. *J. Microsc.* 117, 77–91.
- Glaeser, R.M., Downing, K.H., DeRosier, D.J., Chiu, W., Frank, J., 2007. Data Processing: Images of 3-D Crystals. *Electron Crystallography of Biological Macromolecules*. Oxford University Press, Oxford.
- Grigorieff, N., 2007. FREALIGN: high-resolution refinement of single particle structures. *J. Struct. Biol.* 157, 117–125.
- Hayward, S.B., Glaeser, R.M., 1979. Radiation damage of purple membrane at low temperature. *Ultramicroscopy* 04, 201–210.
- Henderson, R., 1992. Image contrast in high-resolution electron microscopy of biological macromolecules: TMV in ice. *Ultramicroscopy* 46, 1–18.
- Henderson, R., 1995. The potential and limitations of neutrons, electrons and X-rays for atomic resolution microscopy of unstained biological molecules. *Q. Rev. Biophys.* 28, 171–193.
- Henderson, R., 2004. Realizing the potential of electron cryo-microscopy. *Q. Rev. Biophys.* 37, 3–13.
- Henderson, R., Baldwin, J.M., Downing, K.H., Lepault, J., Zemlin, F., 1986. Structure of purple membrane from *Halobacterium halobium*: recording, measurement and evaluation of electron micrographs at 3.5 Å resolution. *Ultramicroscopy* 19, 147–178.
- Henderson, R., Baldwin, J.M., Ceska, T.A., Zemlin, F., Beckmann, E., Downing, K.H., 1990. Model for the structure of bacteriorhodopsin based on high-resolution electron cryo-microscopy. *J. Mol. Biol.* 213, 899–929.
- Howitt, D.G., Glaeser, R.M., Thomas, G., 1976. The energy dependence of electron radiation damage in 1-valine. *J. Ultrastruct. Res.* 55, 457–461.
- Iancu, C.V., Wright, E.R., Heymann, J.B., Jensen, G.J., 2006. A comparison of liquid nitrogen and liquid helium as cryogens for electron cryotomography. *J. Struct. Biol.* 153, 231–240.
- Jesior, J.C., 1982. The grid sectioning technique: a study of catalase platelets. *EMBO J.* 1, 1423–1428.
- Knapik, E., Dubochet, J., 1980. Beam damage to organic material is considerably reduced in cryo-electron microscopy. *J. Mol. Biol.* 141, 147–161.
- Lau, W.C., Baker, L.A., Rubinstein, J.L., 2008. Cryo-EM structure of the yeast ATP synthase. *J. Mol. Biol.* 382, 1256–1264.
- Matsui, Y., Sakai, K., Murakami, M., Shiro, Y., Adachi, S., Okumura, H., Kouyama, T., 2002. Specific damage induced by X-ray radiation and structural changes in the primary photoreaction of bacteriorhodopsin. *J. Mol. Biol.* 324, 469–481.
- Mindell, J.A., Grigorieff, N., 2003. Accurate determination of local defocus and specimen tilt in electron microscopy. *J. Struct. Biol.* 142, 334–347.
- Ravelli, R.B., McSweeney, S.M., 2000. The ‘fingerprint’ that X-rays can leave on structures. *Structure* 8, 315–328.
- Rosenthal, P.B., Henderson, R., 2003. Optimal determination of particle orientation, absolute hand, and contrast loss in single-particle electron cryomicroscopy. *J. Mol. Biol.* 333, 721–745.
- Rubinstein, J.L., Walker, J.E., Henderson, R., 2003. Structure of the mitochondrial ATP synthase by electron cryomicroscopy. *EMBO J.* 22, 6182–6192.
- Stark, H., Zemlin, F., Boettcher, C., 1996. Electron radiation damage to protein crystals of bacteriorhodopsin at different temperatures. *Ultramicroscopy* 63, 75–79.
- Taylor, J.R., 1999. *An Introduction to Error Analysis*, 2nd ed. University Science Books, Sausalito, California.
- Taylor, K.A., Glaeser, R.M., 1976. Electron microscopy of frozen hydrated biological specimens. *J. Ultrastruct. Res.* 55, 448–456.
- Unwin, P.N., Henderson, R., 1975. Molecular structure determination by electron microscopy of unstained crystalline specimens. *J. Mol. Biol.* 94, 425–440.
- Wright, E.R., Iancu, C.V., Tivol, W.F., Jensen, G.J., 2006. Observations on the behavior of vitreous ice at approximately 82 and approximately 12 K. *J. Struct. Biol.* 153, 241–252.
- Yalcin, S., Gurler, O., Gultekin, A., Gundogdu, O., 2006. An analytical expression for electron elastic scattering cross section from atoms and molecules in 1.0 keV to 1.0 MeV energy range. *Phys. Lett. A* 356, 138–145.